Numerical Investigation of High-Speed Turbulent Boundary Layers of Dense Gases

Luca Sciacovelli, Xavier Gloerfelt, Donatella Passiatore, Paola Cinnella, Francesco Grasso

▶ **To cite this version:**

Luca Sciacovelli, Xavier Gloerfelt, Donatella Passiatore, Paola Cinnella, Francesco Grasso. Numerical Investigation of High-Speed Turbulent Boundary Layers of Dense Gases. Flow, Turbulence and Combustion, 2020, Progress in Direct and Large Eddy Simulation, 105 (2), pp.555-579. 10.1007/s10494-020-00133-1 . hal-03660161

HAL Id: hal-03660161
https://hal.science/hal-03660161

Submitted on 5 May 2022

HAL is a multi-disciplinary open access archive for the deposit and dissemination of scientific research documents, whether they are published or not. The documents may come from teaching and research institutions in France or abroad, or from public or private research centers.

L'archive ouverte pluridisciplinaire **HAL**, est destinée au dépôt et à la diffusion de documents scientifiques de niveau recherche, publiés ou non, émanant des établissements d'enseignement et de recherche français ou étrangers, des laboratoires publics ou privés.

Numerical Investigation of High-Speed Turbulent Boundary Layers of Dense Gases

Luca Sciacovelli[1] · Xavier Gloerfelt[1] · Donatella Passiatore[1] · Paola Cinnella[1] · Francesco Grasso[2]

Abstract

High-speed turbulent boundary layers of a dense gas (PP11) and a perfect gas (air) over flat plates are investigated by means of direct numerical simulations and large eddy simulations. The thermodynamic conditions of the incoming flow are chosen to highlight dense gas effects, and laminar-to-turbulent transition is triggered by suction and blowing. In the paper, the behavior of the fully developed turbulent flow region is investigated. Due to the low characteristic Eckert number of dense gas flows ($\mathrm{Ec} = U_\infty^2/c_{p,\infty}T_\infty$), the mean velocity profiles are largely insensitive to the Mach number and very close to the incompressible case even at high speeds. Second-order velocity statistics are also weakly affected by the flow Mach number and the velocity spectra are characterized by a secondary peak in the outer region of the boundary layer because of the higher local friction Reynolds number. Despite the incompressible-like velocity and Reynolds-stress profiles, the strongly non-ideal thermodynamic and transport-property behavior of the dense gas results in unconventional distributions of the fluctuating thermo-physical quantities. Specifically, density and viscosity fluctuations reach a peak close to the wall, instead of vanishing as in perfect gas flows. Additionally, dense gas boundary layers exhibit higher values of the fluctuating Mach number and velocity divergence and a larger dilatational-to-solenoidal dissipation ratio in the near-wall region, which represents a major deviation from high-Mach-number perfect gas boundary layers. Other significant deviations are represented by the more symmetric probability distributions of fluctuating quantities such as the density and velocity divergence, due to the more balanced occurrence of strong expansion and compression events.

Keywords High-speed flow · Turbulent boundary layer · Dense gas

1 Introduction

High-speed flows of gases with complex thermodynamic behavior (often referred to as "real gases") are being paid growing interest from the scientific community due to the manifold applications in aerospace and power generation systems. In this work we focus more particularly on so-called dense gas flows found in several engineering applications, ranging from energy production to high-Reynolds wind tunnels. A typical application is represented by energy conversion cycles like Organic Rankine Cycles (ORC) [see Colonna et al. (2015) for a review] and heat pumps (Zamfirescu and Dincer 2009), but dense gases are also of interest for other applications, e.g., high-Reynolds wind tunnels (Bodenschatz et al. 2014; Berry and Berger 2015; Corliss and Cole 1998). Dense gases are single-phase fluids with complex molecules, operating at pressure and temperature conditions of the same order of their thermodynamic critical point. Examples of fluids with dense gas behavior are heavy fluorocarbons and hydrocarbons, refrigerants and siloxanes (Cramer 1989; Colonna and Silva 2003). The dynamic behavior of such fluids is characterized by means of the fundamental derivative of gas dynamics (Thompson 1971), $\Gamma = 1 + \frac{\rho}{c}\frac{\partial c}{\partial \rho}\Big|_s$ (where c is the speed of sound, ρ the density and s the specific entropy), measuring variations of the sound speed under reversible density perturbations. In gases with sufficiently high molecular complexity (defined as $c_{v,\infty}(T_{cr})/R$, with R the gas constant and $c_{v,\infty}(T_{cr})$ the isochoric heat capacity in the dilute gas limit, measured at the fluid critical temperature T_{cr}), Γ is less than one over an extended range of thermodynamic conditions in the vapor phase. This leads to a reversed variation of the speed of sound in isentropic transformation with respect to perfect gases: c decreases when the gas is compressed and increases when the gas is expanded. Even more dramatic deviations from the perfect gas behavior are expected for gases of the so-called Bethe–Zel'dovich–Thompson (BZT) type, for which a region of negative values of the fundamental derivative Γ (named the "inversion zone") is predicted to appear in the vicinity of the liquid/vapor coexistence curve, on the vapor side. In such conditions, nonclassical waves like expansion shocks become physically admissible [see, e.g., Cinnella and Congedo (2007) and the references therein].

Although a number of numerical studies have investigated in the past dense gas dynamics, most of them are based on simplified models neglecting viscous effects (potential flow or Euler equations) or relying on the Reynolds–Averaged Navier–Stokes equations supplemented with a standard turbulence model (i.e., without any specific calibration or compressibility correction for dense gases). On the other hand, experimental investigations of dense gas flows are particularly difficult and costly, and only very recently some local experimental measurements of pressure and temperature at selected stations in a dense-gas nozzle have been made available (Spinelli et al. 2018), as well as Schlieren photographs (Zocca et al. 2019). Unfortunately, to the authors' best knowledge, no velocity or Reynolds-stress measurements of turbulent dense gas flows have been obtained yet, and the fine details of transitional and turbulent dense gas flows remain largely unknown. In previous research, the present authors have investigated the influence of dense-gas effects in compressible decaying isotropic turbulence (Sciacovelli et al. 2016, 2017) and channel flow (Sciacovelli et al. 2017) configurations by using Direct Numerical Simulations (DNS). Previous studies (Kluwick 1994; Cinnella and Congedo 2007) show that, due to their high specific heat capacities, dense gases are characterized by a strong decoupling of dynamic and thermal fields for any flow configuration. In the turbulent channel flow, this results in temperature fluctuations sensibly smaller than in air, and to a strong correlation between density and pressure fluctuations, in contrast with perfect gases. The complex thermodynamic

behavior of dense gases at thermodynamic conditions corresponding to $\Gamma \approx 0$ also modifies compressibility effects and flow topology: for instance, in freely decaying dense gas turbulence at sufficiently high turbulent Mach numbers, strong compressions are weakened and strong expansions enhanced. The latter may correspond to sheet-like (rather than tube-like) structures, suggesting the formation of expansion eddy shocklets. These phenomena are not observed in confined wall-bounded configurations like turbulent channel flows, because of the smaller turbulent Mach numbers. For dense-gas channel flows, the most significant differences are related to the peculiar evolution of the temperature- and density-dependent transport properties: the temperature variations being small, viscosity and thermal conductivity essentially follow the density profiles, resulting in a liquid-like behavior. At such conditions, variable property scalings like the van Driest or the Trettel and Larsson scaling (Trettel and Larsson 2016) were found to collapse adequately the wall-normal profiles even at large bulk Mach numbers.

In this work we report the first-ever DNS/LES (Large-Eddy Simulation) results for dense-gas (DG) turbulent boundary layers at supersonic Mach numbers. The objective is to understand the role of dense-gas effects for wall-bounded, non-confined and spatially-evolving configurations. For this purpose, a quasi-DNS (a fine wall-resolved implicit LES) is carried out at $M = 6$. This value is much higher than those that are typically encountered in practical dense-gas applications [a remarkable exception being the high-Mach, high-Reynolds NASA Langley CF4 wind tunnel, dismantled in 2017, which used a light perfluorocarbon, CF4, as the working fluid up to $M = 6$ (Berry and Berger 2015)]; nevertheless, such severe operating conditions are of theoretical interest for highlighting dense gas effects. We also report wall-resolved LES results for a lower Mach number ($M = 2.25$), more representative of values encountered in ORC applications, to investigate Mach number effects. In both cases, dense-gas results are compared with perfect-gas (PG) simulations at the same Mach number with the objective to show how the intricate DG behavior affects the turbulent flow statistics and flow topology, and to check the validity of compressibility scalings.

The paper is organized as follows. Details of the governing equations, numerical methods, and computational setup are provided in Sect. 2. The results are discussed in Sect. 3, including the description of first- and second-order statistics, the validity of classical correlations and scalings, and the study of compressibility effects. Lastly, conclusions are drawn in Sect. 4, along with some perspectives for future research.

2 Simulation Details

2.1 Governing Equations

The numerical simulations are based on the single-phase compressible Navier–Stokes equations, solved in a conservative form on Cartesian grids and supplemented by suitable dense-gas constitutive relations. The dense fluid considered in the following simulations is the perfluoro-perhydrophenanthrene, (chemical formula $C_{14}F_{24}$), called hereafter with its commercial name PP11. Its main thermodynamic properties, extracted from Cramer (1989), are provided in Table 1. The model of Martin–Hou Martin and Hou (1955) is used for the thermal equation of state, which is reasonably accurate for the fluid of interest and requires a minimum amount of experimental information for setting the gas-dependent coefficients. The equation of state for the pressure p involves five virial terms and writes:

Table 1 Thermodynamic properties of PP11 ($C_{14}F_{24}$): molecular weight ($\mathcal{M}$), critical temperature (T_{cr}), critical density (ρ_{cr}), critical pressure (p_{cr}), critical compressibility factor (Z_{cr}), boiling temperature (T_b), ratio of ideal-gas specific heat at constant volume over the gas constant ($c_v(T_{cr})/R$) at the critical point, and parameter for the low-density specific heat power law (n)

$\mathcal{M}$	T_{cr}	ρ_{cr}	p_{cr}	Z_{cr}	T_b	$c_v(T_{cr})/R$	n
g mol^{-1}	K	kg m^{-3}	MPa	–	K	–	–
624.11	650.2	627.14	1.46	0.2688	488.15	97.3	0.5776

$$p = \frac{RT}{(v-b)} + \sum_{i=2}^{5} \frac{f_i(T)}{(v-b)^i}, \tag{1}$$

with $b = v_{cr}[1 - (20.533 - 31.883Z_{cr})/15]$ and $f_i(T) = A_i + B_iT + C_i \exp(-kT/T_{cr})$, where $v = 1/\rho$ denotes the specific volume, v_{cr}, T_{cr} and Z_{cr} are the critical specific volume, temperature and compressibility factor, and $k = 5.475$. The coefficients A_i, B_i and C_i depend on the critical temperature and pressure, the critical compressibility factor, the Boyle temperature and one point on the vapor pressure curve. Variations of the low-density specific heat with temperature are modeled by means of a power law:

$$c_{v_\infty}(T) = c_{v_\infty}(T_{cr})\left(\frac{T}{T_{cr}}\right)^n \tag{2}$$

where n is a material-dependent parameter.

In addition to the equations of state, suitable models for the dynamic viscosity μ and thermal conductivity λ of dense gases, which depend on both the gas temperature and pressure (or density), have to be specified. The present results are based on the model of Chung et al. (1988), which incorporates a high-pressure correction term to account for the modification of transport properties values at high pressure (or density) conditions. Such a model has been used in previous works on dense gases (e.g. Cramer and Tarkenton 1992; Cramer and Park 1999) and is considered to be a reasonably accurate semi-theoretical model for calculating the viscosity based on the knowledge of a few thermophysical input parameters [see Poling et al. (2001) for more details], provided that the thermodynamic conditions are far enough from the transcritical region (Kawai et al. 2015), which is the case for the present study. A full description of the model equations can be found in "Appendix" of ref. Sciacovelli et al. (2017).

For the purpose of comparison, numerical results are also presented for air, modeled as a polytropic perfect gas:

$$p = \rho RT \qquad \text{and} \qquad e = c_vT, \tag{3}$$

where $c_v = R/(\gamma - 1)$ is the specific heat at constant volume and γ the specific heats ratio. At the lowest Mach number considered in the study ($M = 2.25$), Sutherland's law is used to model the viscosity μ:

$$\frac{\mu}{\mu_{\text{ref}}} = \left(\frac{T}{T_{\text{ref}}}\right)^{3/2} \frac{T_{\text{ref}} + S_0}{T + S_0} \tag{4}$$

with $\mu_{\text{ref}} = 1.716 \times 10^{-5}$ Pa s, $T_{\text{ref}} = 273.15$ K and $S_0 = 110.4$ K. At the highest Mach number ($M = 6$), viscosity follows a power law, $\mu = \mu_\infty \left(T/T_\infty\right)^{0.7}$, in order to allow direct validation with the DNS results of Franko and Lele (2013). In the present dimensional

calculations, the reference values correspond to a stagnation temperature of 533 K and a stagnation pressure of 37.74 atm. We have noted $(\bullet)_\infty$ the incoming flow quantities. At both Mach numbers, a constant Prandtl number assumption is used to determine the thermal conductivity $\lambda = c_p\,\mu/\mathrm{Pr}$ (with $\mathrm{Pr} = 0.71$).

2.2 Numerical Method

The inviscid flux derivatives in the governing equations are approximated in space by means of centered tenth-order accurate differences. In order to introduce a minimal amount of numerical dissipation while ensuring computational robustness for compressible flow simulations, the centered scheme is supplemented by a high-order nonlinear artificial viscosity term, similar to the approach of Jameson et al. (1981) and Kim and Lee (2001). In our case, we use a blend of second- and tenth-order derivatives approximated by standard central differences. For a 1D problem and a regular Cartesian grid with constant mesh spacing δx (so that $x_j = j\,\delta x$), the semi-discrete tenth-order scheme in space writes:

$$(w_t)_j + \frac{(\delta \mathcal{F})_j}{\delta x} = 0$$

where w is the vector of conservative variables, δ is the classical difference operator over one cell, $\delta(\bullet)_j := (\bullet)_{j+\frac{1}{2}} - (\bullet)_{j-\frac{1}{2}}$, and $\mathcal{F}_{j+\frac{1}{2}}$ is the numerical flux at cell interface $j+\frac{1}{2}$:

$$\mathcal{F}_{j+\frac{1}{2}} = \left[\left(I - \frac{1}{6}\delta^2 + \frac{1}{30}\delta^4 - \frac{1}{140}\delta^6 + \frac{1}{630}\delta^8\right)\mu f - \mathcal{D}\right]_{j+\frac{1}{2}}$$

where $f = f(w)$ is the physical flux, μ is the cell average operator, $\mu(\bullet)_{j+\frac{1}{2}} := \frac{1}{2}\left((\bullet)_{j+1} + (\bullet)_j\right)$, and $\mathcal{D}$ is the numerical dissipation term:

$$\mathcal{D}_{j+\frac{1}{2}} = \rho(A)_{j+\frac{1}{2}}\left[\varepsilon_2 \delta w + \varepsilon_{10}\delta^9 w\right]_{j+\frac{1}{2}}$$

with $\rho(A)$ the spectral radius of the flux Jacobian matrix $A = \partial f/\partial w$, and

$$\varepsilon_{2j+\frac{1}{2}} = k_2 \max(\nu_j \boldsymbol{\Phi}_j, \nu_{j+1}\boldsymbol{\Phi}_{j+1}), \quad \varepsilon_{10j+\frac{1}{2}} = \max(0, k_{10} - \varepsilon_{2j+\frac{1}{2}}),$$

with k_2 and k_{10} adjustable dissipation coefficients. The activation of the low-order term rests on Jameson's pressure-based shock sensor ν (Jameson et al. 1981) combined with Ducros' sensor (Ducros et al. 1999). The sensor is $\mathcal{O}(1)$ in high-divergence regions and tends to zero in vortex dominated regions, which allows the capture of flow discontinuities with minimal damping of the vortical structures inside the boundary layer. Note that, when $k_2 = 0$ and $k_{10} = \frac{1}{1260}$ the preceding method becomes equivalent to a ninth-order accurate upwind scheme. For all computations, we set $k_2 = 2$ and $k_{10} = \frac{1}{1260}$, except for Mach 6 dense-gas case where the value of k_{10} is multiplied by a factor of three (due to the near-wall high density fluctuations that can undermine the robustness of the simulation). Far from flow discontinuities, the spatial scheme has very low phase and dissipation errors, as discussed in Sciacovelli et al. (2016). An assessment of the accuracy of the numerical scheme for freely decaying compressible homogeneous isotropic turbulence can be found in the same reference. The tenth-order dissipation is selective in the wavenumber space, and it affects only wavelengths discretized with less than 6 mesh points. As a consequence, it constitutes a suitable implicit subgrid regularization term for LES simulations (Gloerfelt

and Cinnella 2019), with the capability of seamlessly converging to DNS in smooth flow regions as the grid is refined.

The viscous flux derivatives are approximated by fourth-order accurate central formulae. Time advancement is carried out by means of an explicit four-stage low-storage Runge–Kutta scheme. The non-uniformity of the wall-normal mesh spacing is taken into account by a suitable 1-D coordinate transformation. Near the non-periodic boundaries, the finite-difference stencil for the convective terms is progressively reduced down to the second order, whereas the viscous stress terms are evaluated from the interior points by using fourth-order backward differences.

2.3 Computational Setup

The spatial development of zero-pressure-gradient turbulent boundary layers on a flat plate is simulated for both PP11 and air flows. Two configurations have been selected: a hypersonic TBL at $M = 6$ (HTBL) and a supersonic TBL at $M = 2.25$ (STBL). The higher value of the Mach number does not correspond to a configuration of practical use, but is of theoretical interest for highlighting dense-gas effects in wall turbulence. The lower Mach number is more representative of flow conditions achievable in dense-gas turbines. The free-stream conditions are chosen such that the fundamental derivative of gas dynamics Γ is negative outside of the boundary layer and remains lower than unity close to the wall. This allows to investigate strongly non-ideal thermodynamic effects, although such operating conditions are difficult to reproduce in an experimental facility.

In order to avoid uncertainties associated with turbulent inflow conditions like synthetic turbulence (Wu 2017) or rescaling/recycling (Lund et al. 1998), which have not been tuned for flows governed by dense gas equations of state, laminar inflow conditions are set at the entrance of the computational domain and transition to turbulence is triggered by means of suction/blowing at the wall.

The inlet of the domain corresponds to the leading edge of the flat plate for HTBL simulations, hence unperturbed free-stream conditions are imposed at the upstream boundary. On the contrary, STBL simulations start with a finite laminar boundary layer thickness to save computational time; in this case, the compressible laminar similarity solution is imposed at the inflow. The inlet Reynolds number is $Re_{\delta^*_{\text{in}}} = 1700$ for air and $Re_{\delta^*_{\text{in}}} = 3000$ for PP11, with δ^*_{in} the inlet displacement thickness.

At the wall, no-slip and isothermal conditions are imposed. The wall temperature value is set equal to the laminar adiabatic wall temperature, calculated by means of a generalized compressible Blasius solver (Gloerfelt et al. 2020). This corresponds to a pseudo-adiabatic condition, a common practice in high-speed perfect-gas boundary layer calculations [see, e.g., Table 1 of Ref. Wenzel et al. (2018)]. We verified that, for the dense gas cases, the wall heat flux (made non-dimensional with the outer density, velocity and enthalpy) is of the order of 10^{-6} or less at the plate wall. As a consequence, the flow is much closer to adiabatic conditions than in perfect gas cases and wall cooling/heating effects are not expected to play any significant role. To achieve a turbulent state, the laminar-to-turbulent transition is triggered using a blowing and suction device acting on a small strip of the wall plate, which consists in a time-and-space-dependent wall-normal velocity disturbance of the form:

$$v_w = Af(x)g(z)\left\{ a_{2D}\cos(\omega t) + a_{3D}\cos(\omega t \pm \beta z) + \sum_{m=1}^{5} a_H \cos(\omega t \pm 2m\beta z) \right\} \quad (5)$$

where A, ω and β are the amplitude, the pulsation and the spanwise wavenumber of the fundamental mode. The coefficients a_{2D}, a_{3D} and a_H are used to specify the amplitude of the 2D fundamental mode, 3D fundamental mode and higher-order modes, respectively. Following Franko and Lele (2013), the distributions of the forcing in the streamwise (f) and spanwise (g) directions are defined as:

$$f(x) = e^{-\frac{x-x_0}{2\sigma^2}} \quad \text{and} \quad g(z) = 1 + 0.1\left[e^{-\left(\frac{z-z_w}{z_w}\right)^2} - e^{-\left(\frac{z+z_w}{z_w}\right)^2}\right]$$

The Gaussian strip is centered at x_0 with a half-width σ (such that $\sigma^2 = 0.87\frac{2\pi U_\infty}{\omega\delta^*_{\text{forc}}}$, with δ^*_{forc} the displacement thickness at the forcing location x_0). A small dissymmetry is introduced in the spanwise direction, centered at z_c with width z_w (in all cases $z_w/\delta^*_{\text{forc}} = 6$). The forcing frequency and spanwise wavenumber, as well as the forcing Reynolds number are determined based on a preparatory linear stability analysis (Gloerfelt et al. 2020) and are different for each of the cases. The forcing parameters used in each simulation are reported in Table 2. A validation of the forcing procedure against numerical data from the literature for a turbulent boundary layer at $M = 6$ (Franko and Lele 2013) is reported in "Appendix".

At the upper boundary, one-dimensional nonreflecting characteristic boundary conditions (Thompson 1987) are applied, whereas a simple extrapolation of variables is used at the supersonic/hypersonic outlet. No sponge zones are introduced at the inlet, outlet, and upper boundaries. Lastly, periodic boundary conditions are set in the spanwise direction. Figure 1 illustrates the computational domain and the boundary conditions. For all cases, the Cartesian grid is evenly spaced in the streamwise (x) and spanwise (z) directions, whereas a geometric stretching is applied in the wall-normal direction (y) with a rate of 1.5%.

A summary of the numerical parameters and of the reference conditions is provided in Table 3. The reported boundary layer properties are evaluated at the end of the computational domain and are used to get insight into the resolution of the various simulations. The values of grid sizes in wall units indicate that the perfect-gas simulation at $M = 6$ can be classified as DNS following the standard terminology (see, e.g., Poggie et al. 2015; Wenzel et al. 2018; Zhang et al. 2018) with the caution, commonly accepted in compressible turbulence studies, that eddy shocklets are captured and not resolved. In the dense gas simulations, the characteristic Reynolds numbers are larger than in perfect gas, due to the high density (two orders of magnitude higher than air). As a consequence, strict DNS resolution requirements are more difficult to achieve. For the DG HTBL, the spatial resolution in wall units is somewhat coarser than in the PG case, and corresponds to a quasi-DNS or a

Table 2 Numerical parameters of the forcing function in equation (5) for the different cases

Case	A/U_∞	a_{2D}	a_{3D}	a_H	$\beta\delta^*_{\text{forc}}$	$\omega\delta^*_{\text{forc}}/U_\infty$	$\text{Re}_{\delta^*_{\text{forc}}}$
Air $M = 2.25$	0.01	0	1	0	0.2	0.12	2000
Air $M = 6$	0.002	0	1	0	0.3	0.15	3000
PP11 $M = 2.25$	0.035	0	1.05	0.05	0.3	0.6	3100
PP11 $M = 6$	0.02	1	0.05	0.05	0.3	0.6	1200

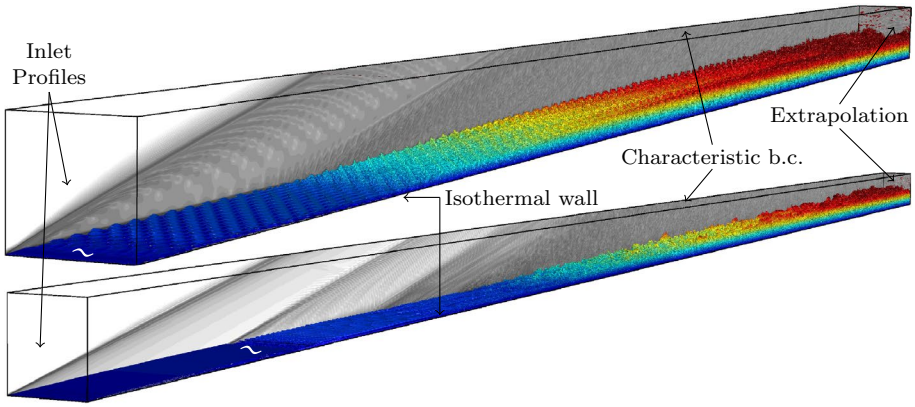

Fig. 1 View of the computational domain for the $M = 6$ air (top) and PP11 (bottom) cases. Instantaneous snapshot of the Q-criterion colored by the distance from the wall, and isocontours of $\log|\nabla\rho|$ on the background planes. The white symbol "~" denotes the location of the suction and blowing forcing

Table 3 Simulation parameters and boundary layer properties at the end of the domain

Fluid	Air		PP11	
M	2.25	6	2.25	6
U_∞ [m/s]	363.6	969.7	78.99	198.8
ρ_∞ [kg/m^3]	0.13	0.13	348.4	348.4
T_∞ [K]	65	65	650.8	646.83
T_w [K]	120.18	422.5	653.4	663.2
Ec_∞	2.03	14.4	5.42×10^{-3}	3.31×10^{-3}
N_x	4000	7700	10000	14336
N_y	210	300	270	320
N_z	140	400	176	280
$\mathrm{Re}_{\delta^*_{\mathrm{in}}}$	1700	0	3000	0
$\mathrm{Re}_{\delta^*_{\mathrm{forc}}}$	2000	3000	3100	1200
Re_θ	4600	5720	9200	4402
δ_{99} [mm]	5.43	5.98	0.132	0.032
θ [mm]	0.46	0.23	0.015	0.0031
H	3.66	13.81	1.51	2.12
Δx^+	11.57	3.76	19.57	8.12
Δy^+_w	0.82	0.26	0.98	0.65
Δy^+_e	10	5.1	24	18
Δz^+	5.63	2.09	12.07	9.77
L_x/δ_{99}	62.5	75.2	75.1	90.1
L_y/δ_{99}	1.75	2.13	1.48	1.75
L_z/δ_{99}	1.06	2.17	0.85	1.56

fine wall-resolved ILES (implicit LES). The spatial resolution has been also evaluated with respect to the wall-normal distribution of the Kolmogorov length-scale $\eta = [\overline{\mu}^3/(\overline{\rho}^3\overline{\varepsilon})]^{\frac{1}{4}}$, where $\overline{\varepsilon}$ is the turbulent kinetic energy dissipation. The values at the wall and at the

boundary layer edges, shown for HTBL simulations in Table 4, confirm the previous statement: despite similar mesh topologies and sizes, resolutions achieved in the DG simulations differ significantly from the PG case, being more unfavorable at the wall and more favorable at the boundary layer edge. The present results may serve as guideline for mesh resolution requirements in future studies of dense gas boundary layers. Dense gas behavior and its influence on mesh resolution requirements are further discussed in the next Section. A recent study of resolution requirements in compressible DNS of spatially-evolving TBL by Poggie et al. (2015) showed that wall-resolved ILES seamlessly converges to DNS as the grid is refined, which gives us confidence in the interpretation of the present results, at least in terms of first and second-order statistics. The PG and DG simulations at $M = 2.25$, on the other hand, are coarser and correspond to the criteria of a wall-resolved ILES. Of note, the perfect gas simulations were found to be in good agreement with reference numerical results of Pirozzoli and Bernardini (2011) (see "Appendix").

To provide a glimpse of the computational cost, we mention that the $M = 6$ simulation for air (924 million points) was run on 7 392 cores and represents approximately 2 millions CPU hours on Intel Xeon 8168 processors. The corresponding simulation for PP11 (1.13 billion points) was split on 16 384 cores and corresponds to approximately 6 millions CPU hours on similar processors.

3 Numerical Results

In the following, numerical results for dense-gas boundary layers are compared with perfect-gas simulations at the same Mach and Reynolds numbers. In the discussion, the main focus is set on the highest Mach number configuration, which exhibits the largest deviations from the PG behavior and for which DNS resolution has been achieved. Wall-resolved LES results at $M = 2.25$ are also presented with the aim of discussing Mach number effects.

3.1 Global Flow Properties and First-Order Statistics

Figure 2 provides an overview of the boundary layer evolution for DG and PG cases. The figure reports the skin friction coefficient distributions along the plate, transformed to equivalent "incompressible" values by means of the Van Driest II transformation (Van Driest 1956):

$$C_{f,\mathrm{inc}} = F_c C_f \tag{6}$$

where

Table 4 Grid resolutions for $M = 6$ simulations, evaluated at the wall and at the boundary layer edge, normalized with respect to the local averaged Kolmogorov scale

Case	$(\Delta x)_w$	$(\Delta y)_w$	$(\Delta z)_w$	$(\Delta x)_e$	$(\Delta y)_e$	$(\Delta z)_e$
Air $M = 6$	$2.7\eta_w$	$0.2\eta_w$	$1.5\eta_w$	$4.3\eta_e$	$3.5\eta_e$	$2.4\eta_e$
PP11 $M = 6$	$6.3\eta_w$	$0.5\eta_w$	$7.5\eta_w$	$1.6\eta_e$	$2.8\eta_e$	$2.1\eta_e$

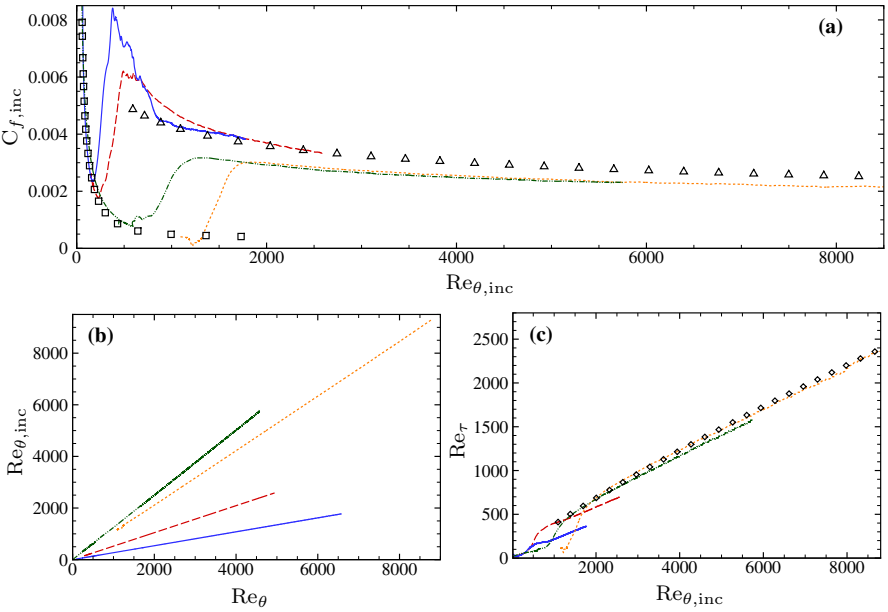

Fig. 2 Evolution of selected properties across the turbulent boundary layers. red dashed line Air $M = 2.25$, blue line Air $M = 6$, orange dotted line PP11 $M = 2.25$, green dash-dotted line PP11 $M = 6$. In panel (**a**), square: Blasius laminar solution, triangle: turbulent correlation $\mathrm{C}_{f,\mathrm{inc}} = 0.024\mathrm{Re}_{\theta,\mathrm{inc}}^{-1/4}$ (Smits et al. 1983). In panel (**c**), diamond: correlation $\mathrm{Re}_{\tau} = 1.13\mathrm{Re}_{\theta}^{0.843}$ (Schlatter and Örlü 2010)

$$\mathrm{C}_f = \frac{\tau_w}{\frac{1}{2}\rho_\infty U_\infty^2}, \qquad F_c = \frac{T_w/T_\infty - 1}{\arcsin^2 \alpha}, \qquad \alpha = \frac{T_w/T_\infty - 1}{\sqrt{T_w/T_\infty\,(T_w/T_\infty - 1)}} \tag{7}$$

as a function of $\mathrm{Re}_{\theta,\mathrm{inc}} = \frac{\mu_\infty}{\mu_w}\mathrm{Re}_\theta$, being $\mathrm{Re}_\theta = \frac{\rho_\infty U_\infty \theta}{\mu_\infty}$ and θ the momentum thickness. The Blasius laminar solution $\mathrm{C}_{f,\mathrm{inc}} = 0.664\,\mathrm{Re}_x^{-1/2}$ and a classical empirical turbulent correlation $\mathrm{C}_{f,\mathrm{inc}} = 0.024\,\mathrm{Re}_{\theta,\mathrm{inc}}^{-1/4}$ (Smits et al. 1983) are also reported for reference. In all cases, the distribution of C_f initially matches the laminar correlation; then it rapidly departs from it and a significant overshoot is visible for PG flow at $M = 6$. The transition path and intensity of the overshoot obtained for the PG flow at $M = 6$ are in very good agreement with (Franko and Lele 2013), as shown in "Appendix". At higher Re, the results are close to the empirical correlation. Similar considerations hold for PG at $M = 2.25$. The DG skin friction distribution follows reasonably well the trend of the turbulent correlation but values are lower, because the van Driest II compressibility correction for the skin friction, derived by integrating the boundary layer equations under PG assumptions, is not suitable for the DG. In practice, the van Driest II law has almost no effect on DG results, since T_w/T_∞ remains close to the unity, as shown later, leading to $F_c \approx 1$. An extension of the transformation to dense gases is not straightforward, due to the complex relations between flow properties in the dense gas. Interestingly, the skin friction distributions at $M = 2.25$ and 6 for the dense gas are very close to each other, with no overshoot at the laminar-to-turbulent transition and almost no influence of the Mach number.

In Fig. 2b, we also report the variation of the incompressible versus compressible momentum-thickness-based Reynolds numbers along the plate for DG and PG boundary

layers. While the range of Re_θ is reasonably similar for DG and PG flows, its incompressible counterpart ($\mathrm{Re}_{\theta,\mathrm{inc}}$) differs substantially. For DG at $M = 2.25$ the compressible and incompressible Reynolds numbers are very close to each other, due to the negligible friction heating and small viscosity variations in the DG. For the $M = 6$ case, $\mathrm{Re}_{\theta,\mathrm{inc}}$ becomes somewhat larger than Re_θ, unlike PG, for which $\mathrm{Re}_{\theta,\mathrm{inc}}$ becomes smaller and smaller as M is increased. Due to the opposite behavior of $\mathrm{Re}_{\theta,\mathrm{inc}}$ in dense and perfect gas flows and to the fact that PG flows remain transitional over a large portion of the flat plate, the region of overlapping $\mathrm{Re}_{\theta,\mathrm{inc}}$ values in the fully turbulent region for DG and PG is almost void. A similar effect is observed for the friction Reynolds number Re_τ, reported in Fig. 2c along with the incompressible correlation of Schlatter and Örlü (2010), $\mathrm{Re}_\tau = 1.13\mathrm{Re}_{\theta,\mathrm{inc}}^{0.843}$. The latter matches very well the DG results, especially at the lowest Mach number, for which the boundary layer evolution is closer to the incompressible behavior. For PG cases, Re_τ is much lower due to the significant friction heating, so that they do not share any common value with DG cases in the fully developed turbulent flow region. For this reason, in the following we choose to compare the wall normal profiles of first- and second-order statistics at iso-Re_θ.

Figure 3 shows selected profiles of first-order statistics in the turbulent region at $\mathrm{Re}_\theta = 4000$. We adopt the semi-locally-scaled wall normal coordinate $y^* = \overline{\rho} y u_\tau^* / \overline{\mu}$, based on the semi-local friction velocity $u_\tau^* = \sqrt{\tau_w / \overline{\rho}}$ (Huang et al. 1995), and focus on thermodynamic and transport properties first. Both for PG and DG, the mean density (panel a) increases from the wall towards the boundary layer edge and, as expected, this effect is more pronounced at the highest Mach number. However, the variations are much smaller in DG, where the ratio of the external to the wall density is about 1.3 at $M = 6$, against a factor of more than 6 for PG at the same conditions. We also notice that the DG density profile exhibits a trend similar to the velocity profile (shown in Fig. 5), with an approximately linear variation in the viscous sublayer and a nearly logarithmic variation in the outer region. This is consistent with previous observations (Sciacovelli et al. 2017) that density is strongly correlated with pressure and, consequently, with velocity in DG flows, whereas it is more correlated with temperature in PG ones. The temperature profiles for PG and DG (panel b) highlight the strong friction heating of the near-wall region for PG flows, where the wall-to-external temperature ratios are approximately 1.8 and 6.5 for the

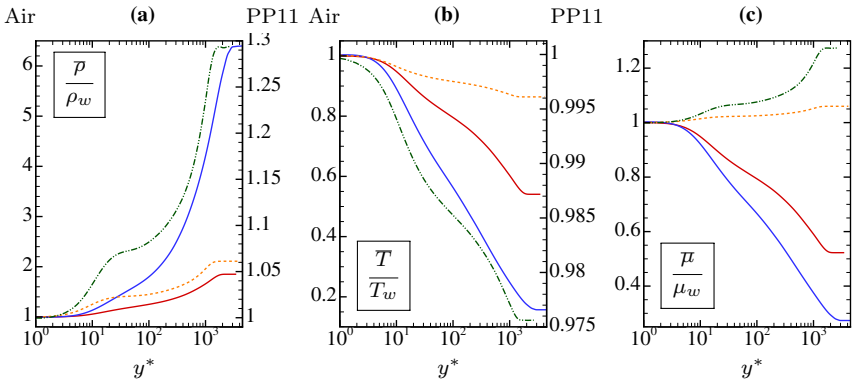

Fig. 3 Wall-normal profiles of selected first-order statistics for Air and PP11, normalized with respect to wall values. **a**, average density; **b**, average temperature; **c**, average viscosity. Red dashed line Air $M = 2.25$, blue line Air $M = 6$, orange dotted line PP11 $M = 2.25$, green dash-dotted line PP11 $M = 6$

$M = 2.25$ and $M = 6$ cases, respectively. These values are in excellent agreement with the predictions of the Walz law (Walz 1969) (reported in "Appendix"). For DG, the temperature also increases toward the wall, but its variations are one to two orders of magnitude smaller, and do not exceed 3% at the highest Mach number. The average viscosity profiles (panel c) follow the trend of the temperature profiles in PG, with the well-known friction-heating increase of viscosity in the wall region. For DG, the viscosity is essentially correlated with density and decreases toward the wall. This opposite behavior has been already observed for compressible turbulent channel flows (Sciacovelli et al. 2017) although, in that case, temperature and density increase from the wall toward the channel centerline. As a consequence, the average viscosities exhibit opposite variations with the wall distance with respect to the present boundary layer flows.

Figure 4 reports the profiles of the mean molecular Prandtl number and of the fundamental derivative of gas dynamics for DG boundary layers at $\mathrm{Re}_\theta = 4000$. The former varies across the boundary layers and decreases monotonically from values higher than 2 in the outer region to 1.95 and 1.53 at the wall for $M = 2.25$ and $M = 6$, respectively. As a consequence, the thermal boundary layer is somewhat thinner than the dynamic one in DG cases. The fundamental derivative also varies across the boundary layer and reaches positive values at the wall, mostly due to density variations. Nevertheless, a region of negative values of $\overline{\Gamma}$ persists in the outer region of the boundary layer, characterized by supersonic flow conditions (vertical lines on the same picture indicate the location of the sonic points in the boundary layer profiles). Such a region is more extended for the lowest Mach number case, for which density variations (hence, $\overline{\Gamma}$ variations), are smaller.

The velocity profiles for all cases are plotted in Fig. 5 using the classical incompressible and van Driest scalings:

$$u^+ = \frac{\overline{u}}{u_\tau} = \frac{\overline{u}}{\sqrt{\tau_w/\rho_w}}, \qquad u^*_{\mathrm{VD}} = \frac{u_{\mathrm{VD}}}{u^*_\tau} = \frac{1}{\sqrt{\tau_w/\overline{\rho}}} \int_0^{\overline{u}} \sqrt{\frac{\overline{\rho}}{\rho_w}}\, \mathrm{d}u \tag{8}$$

For PG, the velocity profiles depend on the Mach number and deviate from the classical incompressible law of the wall (panel a). The discrepancy of u^*_{VD} with respect to the incompressible logarithmic law (panel b) comes from the use of the semi-local wall coordinate y^*. A better behavior is recovered when plotting against y^+ (see "Appendix", Fig. 16c), but the results at different Mach numbers do not fully collapse anymore. For DG, the velocity

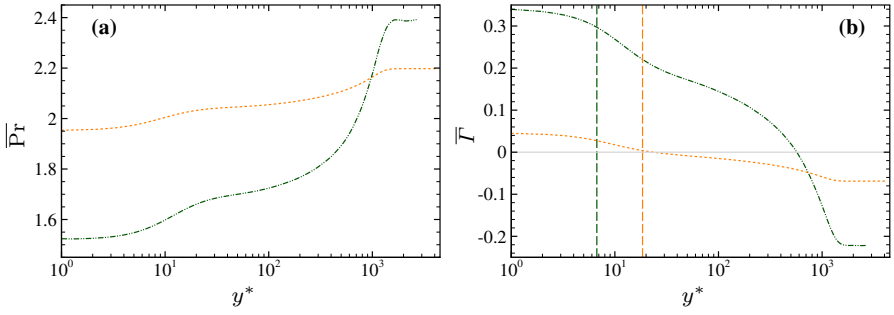

Fig. 4 Wall-normal profiles of the average Prandtl number **a** and fundamental derivative of gas dynamics **b** for PP11. Vertical dashed lines in panel **b** denote the sonic lines for the two cases. Orange dotted line PP11 $M = 2.25$, green dash-dotted line PP11 $M = 6$

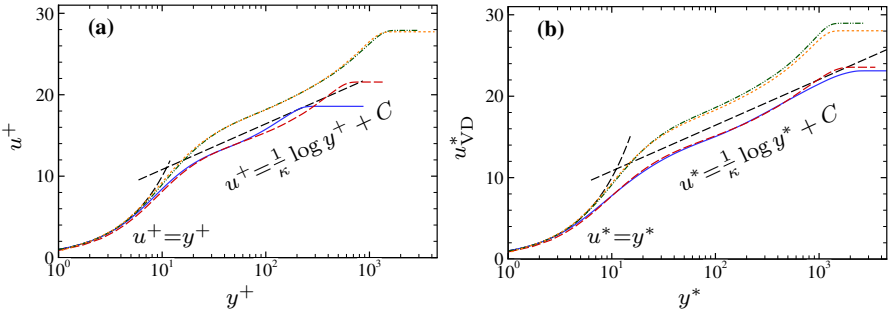

Fig. 5 Velocity profiles for Air and PP11: (**a**), wall scaling; (**b**), semi-local Van-Driest scaling. Black dashed lines denote the linear and logarithmic laws, with $\kappa = 0.41$ and $C = 5.2$. Red dashed line Air $M = 2.25$, blue line Air $M = 6$, orange dotted line PP11 $M = 2.25$, green dash-dotted line PP11 $M = 6$

profiles at various Mach numbers are very close to each other using the incompressible scaling, and weakly sensitive to the van Driest scaling, due to the weak variations of $\overline{\rho}$ across the boundary layer. As noticed in previous studies (Cinnella and Congedo 2007; Sciacovelli et al. 2017), this effect results from the very low Eckert number of DG flows ($\mathrm{Ec}_\infty = U_\infty^2/(c_{p,\infty}T_\infty)$, see Table 3), leading to substantial decoupling of the dynamic and thermal boundary layers and to significantly smaller friction heating of the boundary layer compared to PG. The slope of the logarithmic region matches well the standard value of the von Kármán constant $\kappa = 0.41$ but the intercept constant is higher than the incompressible value ($C = 5.2$). A possible explanation for this discrepancy may reside in the definition of the scaling variables: for PG, turbulent fluctuations of fluid properties tend to vanish at the wall, so that averages of products/ratios of flow properties do not differ much from products/ratios of the average values. This is not true for DG flows, as discussed in the following.

3.2 Second-Order Statistics

The wall-normal profiles of the streamwise turbulent intensity u_{rms} (i.e., the root mean square—rms—streamwise velocity fluctuations) are reported in Fig. 6 using both the

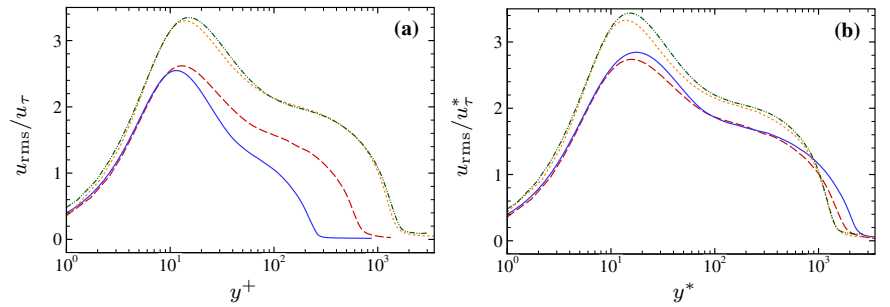

Fig. 6 Wall-normal profiles of streamwise Reynolds stress, using the wall scaling (**a**) and semi-local scaling (**b**). Red dashed line Air $M = 2.25$, blue line Air $M = 6$, orange dotted line PP11 $M = 2.25$, green dash-dotted line PP11 $M = 6$

incompressible and semi-local scaling. As expected, the latter succeeds in collapsing results at different Mach numbers for PG and has little effect on DG profiles, which are very close to each other in both scalings and for all Mach numbers. The peak location corresponds to $y^*\approx 11 \div 12$ in all cases. However, DG results are characterized by a higher peak in the inner region and by a plateau in the outer one, and exhibit a general trend reminiscent of high Reynolds incompressible boundary layers. Similar considerations hold for the other Reynolds stresses (not shown).

Second-order statistics for the fluctuating thermodynamic properties are reported in Fig. 7. The temperature fluctuations (panel a) exhibit similar trends for PG and DG, with a peak located at $y^*\approx 12$, i.e. close to the turbulent intensity peak. As expected, the values observed in DG are much lower (two orders of magnitude) than in PG, so that the flow can be considered as isothermal to a first approximation and the variations of all thermodynamic quantities can be explained in terms of density fluctuations only. The latter exhibit striking differences with respect to PG flows (panel b): while $\rho_{\mathrm{rms}}/\rho_w$ reaches a maximum in the outer region (the peak value being close to 1 at $M = 6$), it decreases smoothly and almost monotonically when departing from the wall for DG. A similar effect has been also observed in compressible turbulent channel flows of dense gases and can be explained by the wall-normal variation of the mean density and by the slope of the constant-temperature and constant-entropy curves in a Clapeyron (p–v) diagram. For gases governed by real-gas equations of state like the Martin–Hou equation used in this study it can be shown that $\rho_{\mathrm{rms}}/\overline{\rho} \approx (p_{\mathrm{rms}}/\overline{p})/(\partial p/\partial \rho)_T$ [see Sciacovelli et al. (2017) for more details]. Due to the different trend of the mean density, however, the rms density profile is flatter in boundary layer flows, whereas it exhibits a well-pronounced peak at the wall in channel flows. Overall, despite the DG flow occurring at thermodynamic conditions of the same order of magnitude of the critical point, the density fluctuations remain small compared to the average density and Morkovin's condition $\rho_{\mathrm{rms}}/\overline{\rho} \ll 1$ is well respected. Viscosity fluctuations (panel c) are clearly correlated with temperature fluctuations for the PG and with density fluctuations for the DG. It is worth noting that, at the wall, they are strictly zero for the PG (for which $\mu_w = \mu(T_w) = \text{const.}$), whereas they are maximum for the DG. The strong density and viscosity fluctuations at the wall have an impact on the wall friction τ_w and friction velocity u_τ, leading to different possible definitions.

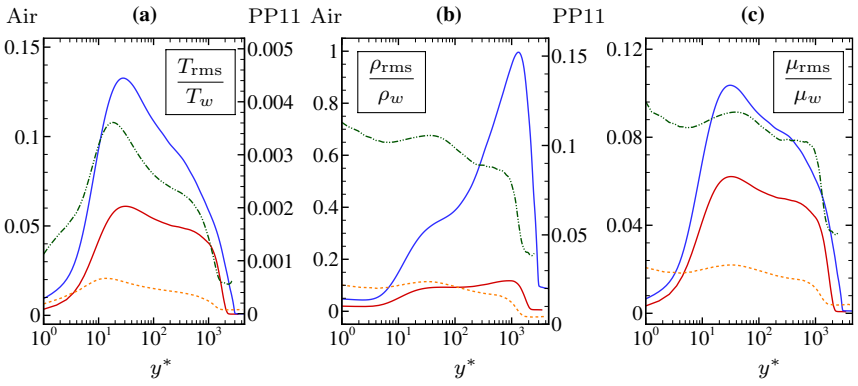

Fig. 7 Wall-normal profiles of selected second-order statistics for Air and PP11, normalized with respect to wall values. **a**, rms temperature; **b**, rms density; **c**, rms viscosity. Red dashed line Air $M = 2.25$, blue line Air $M = 6$, orange dotted line PP11 $M = 2.25$, green dash-dotted line PP11 $M = 6$

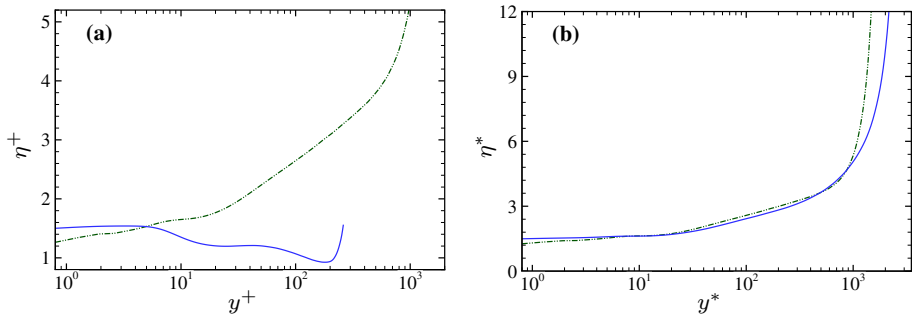

Fig. 8 Kolmogorov length scale with incompressible (**a**) and semi-local (**b**) wall scaling across turbulent boundary layers at $M = 6$: blue line Air, green dash-dotted line PP11

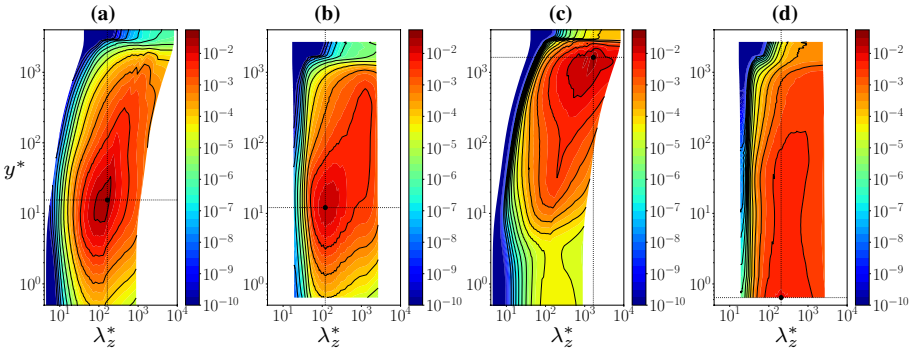

Fig. 9 Premultiplied spanwise spectra of the streamwise velocity fluctuations $k_z E_{uu}(k_z)/U_\infty^2$ (**a**, **b**) and of the density fluctuations $k_z E_{\rho\rho}(k_z)/\rho_\infty^2$ (**c**, **d**) for Air (**a**, **c**) and PP11 (**b**, **d**). The vertical and horizontal black lines denote the location of the peaks

The unconventional variation of the fluid properties has an impact on the characteristic flow scales and, consequently, on the spatial resolution obtained in the simulations. The smallest motions scale with the Kolmogorov length scale η, reported in Fig. 8 in both incompressible and compressible scalings. For both gases, η^+ is close to the incompressible value 1.5 at the wall. However, η^+ reaches a minimum close to the boundary layer edge for PG, due to the decreasing mean viscosity, whereas it monotonically increases in DG, due to the liquid-like viscosity profile. Application of the semi-local scaling allows to recover a trend similar to the incompressible limit for PG, while it does not alter much the DG results, as already observed for other flow properties. As expected (Smits et al. 2011), η^+ remains almost constant in the near-wall region (say, $y^* < 30$), then increases with the wall distance becoming quite large in the non-turbulent region.

For a better understanding of the near-wall turbulent structures, we report in Fig. 9 the fluctuating streamwise velocity and density premultiplied spanwise spectra across the boundary layer for $M = 6$ as a function of the spanwise wavelength λ_z^*. Using the semi-local scaling, the small-scale peak corresponding to the characteristic streaks spacing is centred around $\lambda_z^* \approx 120$ and $y^* \approx 12$ in the velocity spectra for both PG and DG. A larger-scale, outer peak is visible for the DG at $\lambda_z^* \approx 10^3$ and $y^* \approx 200$ (corresponding to $y/\delta_{99} \approx 0.2$), in accordance with reference data for incompressible boundary layers at similar Reynolds

numbers [see, e.g., results in Eitel-Amor et al. (2014) for $\mathrm{Re}_\theta = 4400$]. On the other hand, a different spectral behavior is obtained for the density fluctuations. Specifically, the peak of $k_z E_{\rho'\rho'}$ is located at the boundary layer edge for PG, whereas it is at the wall for DG; this is consistent with the different distributions of the wall-normal ρ_{rms} profiles, as shown in Fig. 7b.

3.3 Compressibility Effects

The preceding discussion of first and second-order statistics shows that, in high-speed DG boundary layers, most flow quantities are largely insensitive to the freestream Mach number and exhibit a behavior similar to incompressible boundary layers. Nevertheless, the flow is characterized by strong fluctuations of the fluid properties in the near-wall region. In order to investigate the role and nature of compressibility effects in DG TBL, we report in Fig. 10 the wall-normal profiles of the turbulent and rms Mach number, defined as $M_t = u_{\mathrm{rms}}/\overline{c}$ and $M_{\mathrm{rms}} = (u/c)_{\mathrm{rms}}$. The turbulent Mach number (panel a) is considerably higher in DG flows with respect to PG at the same M_∞, due to the thinner boundary layer. In particular, the values reached in the neighborhood of the turbulent intensity peak at $M = 6$ are sufficiently high ($M_{t,\max} > 0.5$) to enable the formation of eddy shocklets. Even when M_t is lower than this threshold, the existence of eddy shocklets is not excluded (Duan et al. 2011), since the instantaneous Mach number can be much higher. The profiles of the rms Mach number (panel b) are considerably different for PG and DG at $M = 6$. In PG, the peak in the outer region is greater than the one located in the production region, due to significant fluctuations of the temperature and speed of sound (not shown). The opposite is observed in DG since fluctuations of the thermodynamic properties are globally smaller and M_{rms} is mostly driven by u_{rms}. The outer peak is strongly attenuated for both DG and PG at $M = 2.25$.

In the following we focus on the hypersonic cases. Figure 11 shows the probability density functions (pdf) of selected quantities at a wall-normal location corresponding approximately to the peak of u_{rms} and another one in the outer logarithmic layer. More precisely, the pdf are extracted along spanwise meshlines and for several time instants at $y^* = 11$ and $y^* = 138$ for DG, and at $y^* = 10$, $y^* = 157$ for air. Kernel density estimates of the pdf are obtained by using a total of about 4 million samples. The pdfs of the Mach number (panel a) are significantly skewed toward supersonic values, especially for DG, the right tail being very close to the free-stream Mach value. As a consequence, the probability of supersonic

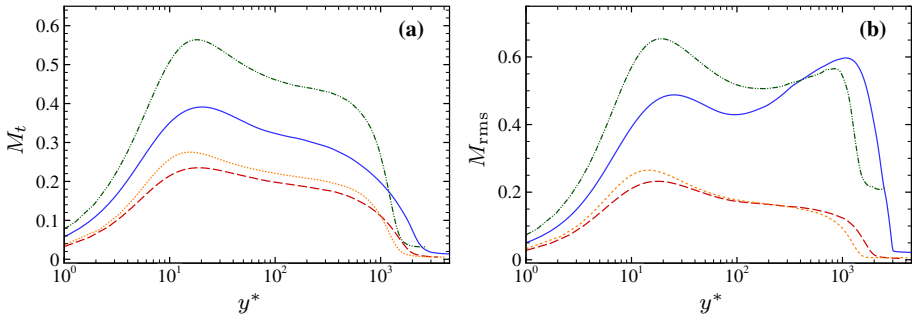

Fig. 10 Wall-normal evolutions of turbulent Mach number (**a**) and rms Mach number (**b**). Red dashed line Air $M = 2.25$, blue line Air $M = 6$, orange dotted line PP11 $M = 2.25$, green dash-dotted line PP11 $M = 6$

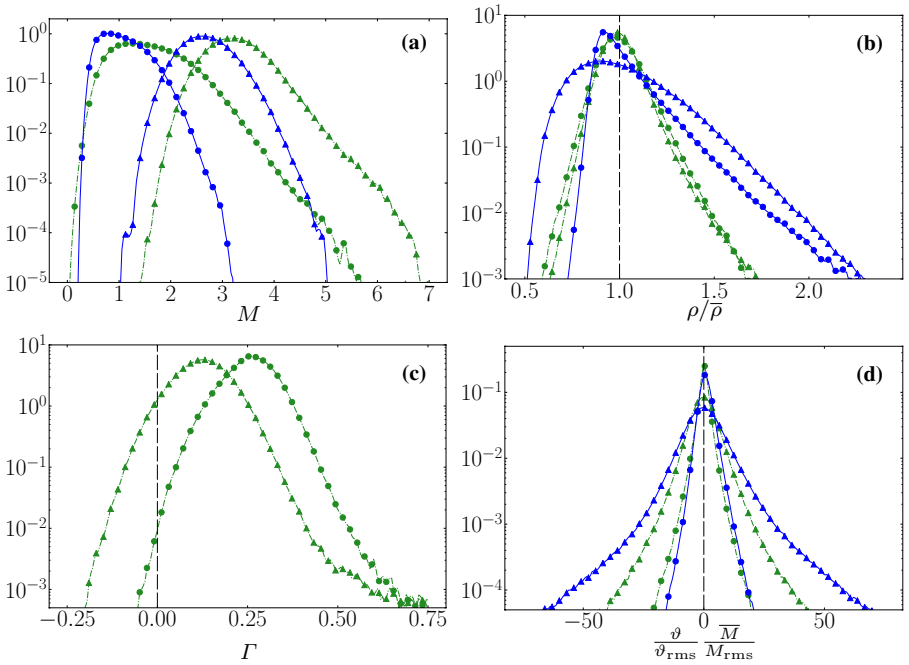

Fig. 11 Probability density functions of the Mach number **a**, normalized density **b**, fundamental derivative of gas dynamics **c** and normalized dilatation **d** for air and PP11. Blue line Air $M = 6$, green dash-dotted line PP11 $M = 6$. Two vertical locations are considered: near the wall ($y^* = 10$ for air and $y^* = 11$ for PP11), circle symbols; in the logarithmic region ($y^* = 157$ for air and $y^* = 138$ for PP11), triangle symbols

local events is rather high even in the inner region of the TBL. In panel b we report the pdf of the fluid density (normalized with the local average) at the same locations. Contrary to the Mach number, the pdf are much more symmetric for DG, whereas states characterized by density values above the average have a much higher probability in PG. Additionally, the width of the pdf is approximately constant for DG, whereas it tends to become wider when y^* increases for PG. If a normalization with respect to the wall density is adopted instead of the local average, then a wider spread of density values is observed for the location nearest to the wall in DG, whereas the opposite is true for PG. This is consistent with the trends observed for the wall-normal profiles of $\rho_{\mathrm{rms}}/\rho_w$ (Fig. 7b). The pdf of the fundamental derivative Γ for PP11, displayed in Fig. 11c, shows that, even if $\overline{\Gamma}$ becomes positive near the wall, instantaneous negative values are still present at $y^* = 10$, i.e. close to the region where M_t peaks. More generally, most thermodynamic states in the flow correspond to $\Gamma \approx 0$. In such conditions, expansion and compression events tend to become equally probable even in the absence of nonclassical BZT effets, as discussed in Sciacovelli et al. (2016, 2017). In Fig. 11d, we report the pdf of the velocity divergence ($\vartheta = \nabla \cdot \mathbf{u}$), often used in the literature to discriminate the preferential occurrence of compression/expansion events. The values are normalized with the rms divergence and the local mean and rms Mach number to ease comparisons between different fluids and locations. Given the low M_t reached in PG, the pdf is obviously symmetric at both the wall distances. For DG, the local Mach numbers are higher, and they would correspond to a pdf skewed toward negative values in PG homogeneous isotropic turbulence. In the DG, however, the pdf remains

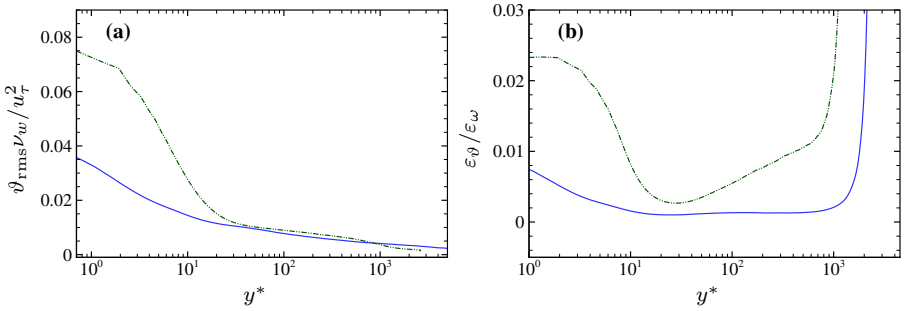

Fig. 12 Wall-normal distributions of normalized rms dilatation (**a**) and ratio of dilatational to solenoidal turbulent dissipation for $M = 6$ cases. Blue line Air $M = 6$, green dash-dotted line PP11 $M = 6$

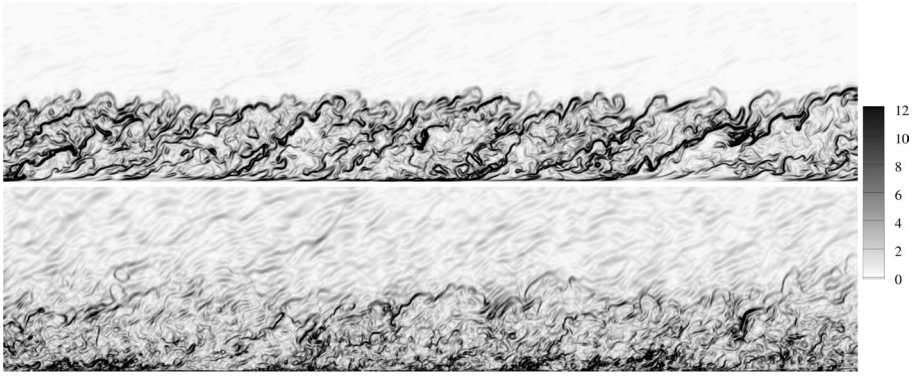

Fig. 13 Instantaneous snapshots of normalized numerical Schlieren $|\nabla\rho|/(\overline{\rho}/\delta_{99,\mathrm{end}})$ for Air (top) and PP11 (bottom) at $M = 6$

well symmetric, consistently with preceding observations of DG homogeneous isotropic turbulence at a similar M_t (Sciacovelli et al. 2017).

Figure 12 reports the wall-normal distributions of the normalized rms dilatation ϑ, as well as the dilatational-to-solenoidal turbulent dissipation ratio $\varepsilon_\vartheta/\varepsilon_\omega$, where $\varepsilon_\vartheta = \frac{4}{3}\mu\overline{\vartheta^2}$ and $\varepsilon_\omega = 2\mu\overline{\omega^2}$ (Huang et al. 1995) ($\omega = |\nabla \times \mathbf{u}|$). Of note, this ratio tends rapidly to infinity outside the boundary layer, the vorticity of the freestream being zero. In DG, near-wall values of the dilatation fluctuations are almost twice those of the PG, which is consistent with the high density fluctuations in the vicinity of the wall. Overall, the contribution of the dilatational dissipation is more significant in a DG boundary layer, and the differences are particularly marked in the inner region and in the wake region. This seems consistent with the highest instantaneous values of the Mach number observed in DG, which increase the probability of eddy shocklets with respect to PG.

In order to provide a global view of the flow topology, we show instantaneous snapshots of the magnitude of the density gradients and of the velocity divergence in Figs. 13 and 14, respectively. The density gradients are normalized by $\overline{\rho}/\delta_{99,\mathrm{end}}$ to obtain comparable ranges for the two flows. The numerical Schlieren for the PG flow exhibits elongated, sheet-like structures corresponding to high-density-gradients ejection events moving towards the boundary layer edge. On the contrary, the high-$|\nabla\rho|$ spots for the DG flow are located near

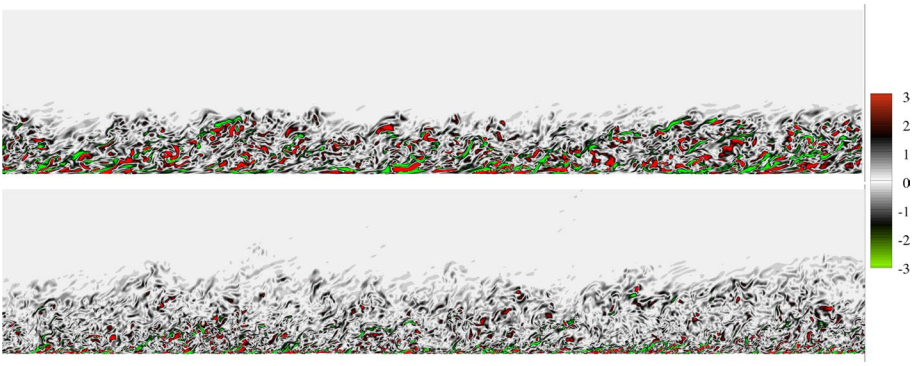

Fig. 14 Instantaneous snapshots of normalized velocity divergence $\vartheta/\vartheta_{\mathrm{rms}}\overline{M}/M_{\mathrm{rms}}$ for Air (top) and PP11 (bottom) at $M = 6$

the wall (in a region where the rms density is also at its maximum), whereas sheet-like structures in the outer region (where $\overline{\Gamma} < 0$) are more sporadic and intermittent. Such spots do not seem to be preferentially associated to expansion or compression events, which are shown to be almost equally likely for both flows. With the aim of relating the occurrence of strong density gradients with expansion/compression events, joint pdfs of the velocity divergence and magnitude of the density gradients are reported in Fig. 15. A weak correlation is noted, as indicated by the low values of the Pearson coefficients r_p (reported in the figure), which give a measure of the linear relationship between the two datasets. The symmetry of the joint pdf for the DG shows that density gradients are not preferentially correlated to compression nor expansion events, whereas a slight correlation with expansion events is noted for the PG, more marked near the wall. Therefore, we conclude that the Schlieren-like illustrations are not representative of the presence of shocklets; for the PG, they rather show the sharp edges of the bulge structures in the outer flow. This picture is strongly altered for the DG, where the density variations are more uniform across the layer and intense events are located close to the wall.

4 Conclusions

In this paper, we reported for the first time high-fidelity numerical simulations of supersonic and hypersonic boundary layers of dense gas (DG) at $M = 2.25$ and $M = 6$. The working fluid selected for the study is the heavy fluorocarbon PP11, already considered in previous studies of decaying homogeneous isotropic turbulence and turbulent channel flows. The calculations were conducted by using a high-order numerical solver and advanced thermodynamic and transport-property models. The dense-gas results are compared with perfect gas (PG) results generated at the same Mach and Reynolds numbers.

For the dense gas, the complex thermodynamics and transport-property variations play a crucial role. Most of the observed effects are due to the much higher molecular complexity of the dense gas, leading to an increase of more than one order of magnitude of the heat capacity compared to light gases like air and, consequently, to much smaller Eckert numbers. In such conditions, temperature variations are nearly negligible throughout the flow field and friction heating is very small even at hypersonic conditions. Due to the substantial

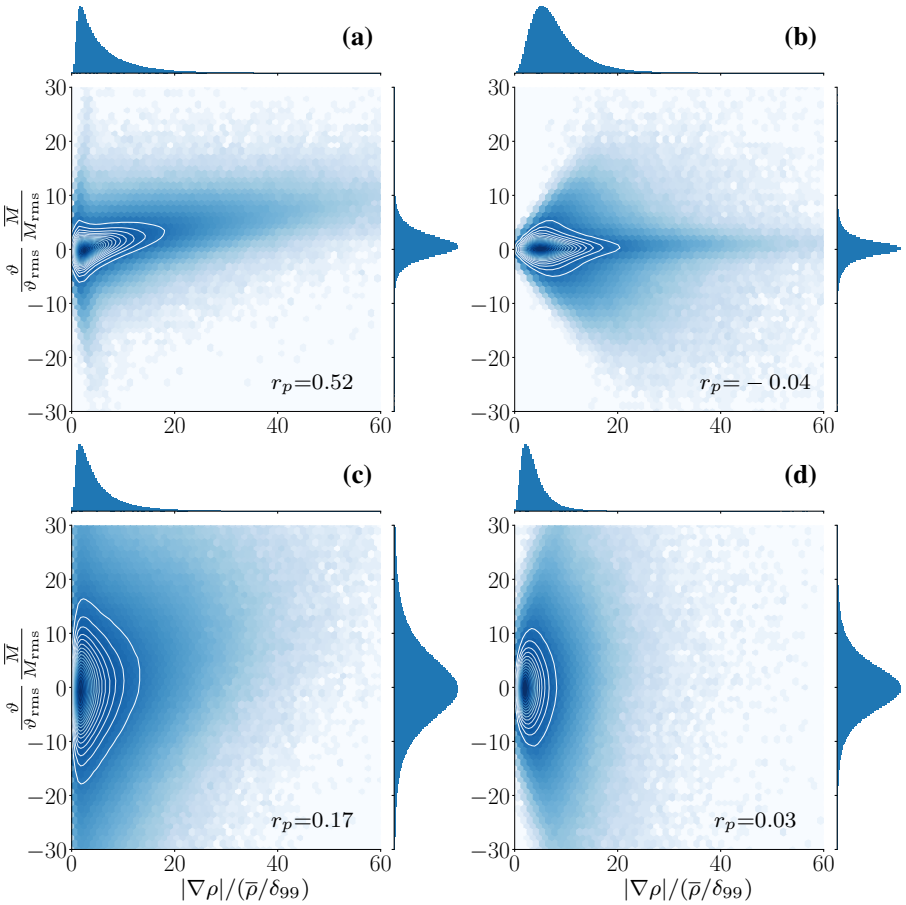

Fig. 15 Joint probability density functions for Air (**a**, **c**) and PP11 (**b**, **d**) at $M = 6$ near the wall (**a**, **b**; $y^* = 10$ for Air and $y^* = 11$ for PP11) and in the logarithmic region (**c**, **d**; $y^* = 157$ for Air and $y^* = 138$ for PP11)

decoupling of the thermal and dynamic boundary layer, the thickening rate of the boundary layer in the dense gas is close to that of an incompressible flow and dynamic quantities are weakly sensitive to the Mach number. On the contrary, wall-normal profiles of mean thermodynamic and transport properties depend on the Mach number, although the amplitude of variation across the boundary layer is much smaller than in perfect gas boundary layers. Specifically, the wall temperature is less than 3% greater than the free-stream temperature for the DG boundary layer at $M = 6$, against a factor close to 7 observed for air at similar conditions. Similarly, the wall density is reduced by less than 25% in the dense gas, against a factor of more than 6 in the PG, and variations of the fluid viscosity across the boundary layer are also greatly reduced and amount to less than 30% for the highest Mach number. Additionally, since the viscosity mostly depends on density in DG conditions (instead of temperature, like in PG), it exhibits an opposite trend across the boundary layer; namely, it decreases when approaching the solid wall. Both of the above-mentioned effects lead to higher local Reynolds numbers, as shown by the velocity spectra, where an outer peak is

present for the DG. The velocity profiles and turbulent intensities are almost unaffected by the Mach number, although further work is probably required to adapt compressible wall scalings, originally derived for perfect gases, in order to improve the matching of dense gas results with incompressible references. Indeed, significant differences are observed for the density and viscosity fluctuations, which reach a maximum near the wall in DG instead of vanishing as in PG. The reduced thickening of the DG boundary layer also leads to a more extended supersonic region than perfect gases and to higher turbulent and fluctuating Mach numbers. Probability density functions of the Mach number clearly show that more frequent supersonic events occur within the DG boundary layers. The analysis of the dilatational events provides a first view of the peculiar behavior in the dense-gas regime. In particular, inspection of the instantaneous divergence fields and their pdf distributions shows that expansion and compression events are rather balanced, differently from the perfect gas. Schlieren-like representations, often used to exhibit the compressive character of the flow, are weakly correlated to compression and expansion events. They, however, depict very different compressibility effects on the boundary layer structure. Sharp bulges dominate the outer flow in PG, whereas density variations are severely attenuated in the outer region of the DG boundary layer, where values of the fundamental derivative of the gas dynamics are close to zero. On the contrary, a strong dilatational activity is located in the near-wall region. Further work is required to better understand how the peculiar compressibility effects may affect the turbulent structures or the Mach wave radiation. The definition of appropriate scalings to ease comparisons with perfect gases and with the incompressible limit may help in this endeavour.

Acknowledgements This work was granted access to the HPC resources of IDRIS and TGCC under the allocation 2018-7332 and 2018-1736 made by GENCI (Grand Equipement National de Calcul Intensif). We also acknowledge TGCC for awarding access to the Joliot-Curie supercomputer under the allocation "Grands Challenges" gch032.

Compliance with Ethical Standards

Conflict of interest The authors declare that they have no conflict of interest.

Appendix: Validations

In this appendix, we present validations of our numerical solver against well-established literature results for perfect-gas (air) high-speed boundary layers at $M = 2.25$ and 6. The simulation at $M = 2.25$ is compared to the DNS data of Pirozzoli and Bernardini (2011). This study focused on the fully turbulent flow behavior and adopted a rescaling/recycling strategy to shorten the computational domain required to achieve fully-developed turbulence. Sutherland's law was used to model the viscosity, along with a constant Prandtl number hypothesis. Figure 16 shows wall-normal profiles of selected flow statistics for the present PG ILES and the DNS of Pirozzoli and Bernardini (2011). An excellent agreement is observed.

The calculation at $M = 6$ has been performed in the same conditions and with the same thermodynamic and transport-property models as the DNS study of Franko and Lele (2013), except that our computational domain is much longer to achieve a fully turbulent state. These authors focused their analysis on the transition mechanisms, so that a comparison is possible only in the transitional regime. Another difference in our

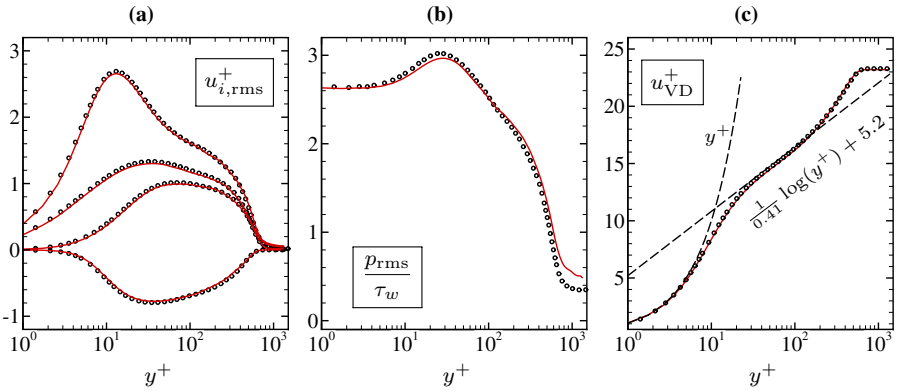

Fig. 16 Wall-normal profiles of Reynolds stresses (**a**), normalized wall pressure (**b**) and Van Driest-scaled streamwise velocity profile (**c**), for current ILES of Air at $M = 2.25$ (lines) and Pirozzoli and Bernardini (2011) (symbols), extracted at $\mathrm{Re}_\tau = 580$

numerical setup is that the inlet of the domain corresponds to the leading edge of the flat plate, whereas Franko and Lele (2013) started with a finite laminar boundary layer thickness, such that the Reynolds number based on the inflow displacement thickness, δ^*_{in}, F&L, is 3000. For the comparisons in Fig. 17, we use this displacement thickness as reference (δ^*_{in}, F&L $= \delta^*_{\mathrm{ref}}$). Panel a shows that the distribution of the skin friction coefficient for the present and the reference calculation are in excellent agreement. The present simulation finally reaches a fully developed turbulent state where C_f follows the trend of classical skin friction correlations (see Sect. 3). Selected velocity profiles at various stations in the laminar, transitional, and nearly turbulent flow regimes are reported on panel b of the same figure. Once again, the present results match remarkably well the reference data, thus confirming the quality of the present simulations.

Finally, in Fig. 18, we compare temperature profiles from the present PG simulations at $M = 2.25$ and $M = 6$ at $\mathrm{Re}_\theta = 4000$ with the classical temperature law of Walz (1969). The numerical results are found to match very well the analytical model.

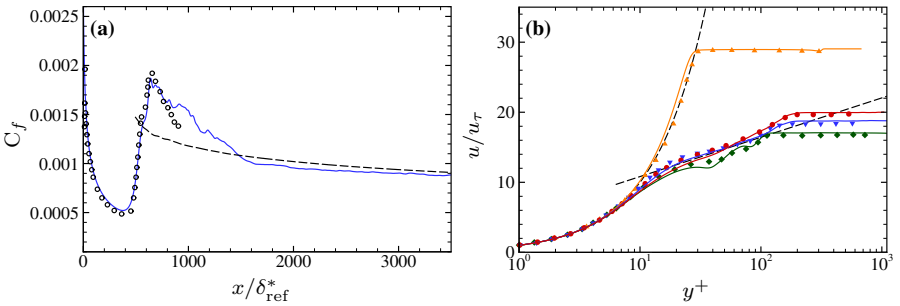

Fig. 17 Skin friction coefficient **a** blue line present DNS; circle DNS of Franko and Lele; dotted line White's turbulent correlation. Mean streamwise velocity profiles **b** present DNS (solid lines) and Franko and Lele (2013) (symbols) at locations $x/\delta^*_{\mathrm{ref}} = 400$ (orange line, orange triangle), 650 (green line, green diamond), 800 (blue line, blue inverted triangle), and 950 (red line, red circle)

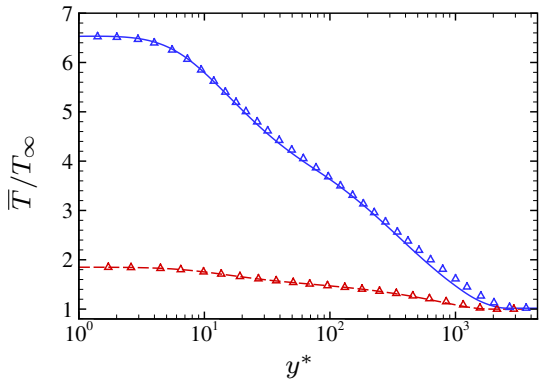

Fig. 18 Normalized temperature profiles for PG runs (lines) and prediction from Walz's law (Walz 1969) (symbols) at $\mathrm{Re}_\theta = 4000$. Red dashed line Air $M = 2.25$, blue line Air $M = 6$

References

Berry, S., Berger, K.: Nasa langley experimental aerothermodynamic contributions to slender and winged hypersonic vehicles. In: 53rd AIAA Aerospace Sciences Meeting, p. 0213 (2015)

Bodenschatz, E., Bewley, G.P., Nobach, H., Sinhuber, M., Xu, H.: Variable density turbulence tunnel facility. Rev. Sci. Instrum. **85**(9), 093908 (2014)

Chung, T., Ajlan, M., Lee, L., Starling, K.: Generalized multiparameter correlation for nonpolar and polar fluid transport properties. Ind. Eng. Chem. Res. **27**(4), 671–679 (1988)

Cinnella, P., Congedo, P.: Inviscid and viscous aerodynamics of dense gases. J. Fluid Mech. **580**, 179–217 (2007)

Colonna, P., Silva, P.: Dense gas thermodynamic properties of single and multicomponent fluids for fluid dynamics simulations. J. Fluids Eng. **125**(3), 414–427 (2003)

Colonna, P., Casati, E., Trapp, C., Mathijssen, T., Larjola, J., Turunen-Saaresti, T., Uusitalo, A.: Organic Rankine cycle power systems: from the concept to current technology, applications, and an outlook to the future. J. Eng. Gas Turbines Power **137**(10), 100801 (2015)

Corliss, J., Cole, S.: Heavy gas conversion of the nasa langley transonic dynamics tunnel. In: 20th AIAA Advanced Measurement and Ground Testing Technology Conference, p. 2710 (1998)

Cramer, M.: Negative nonlinearity in selected fluorocarbons. Phys. Fluids A **1**(11), 1894–1897 (1989)

Cramer, M., Park, S.: On the suppression of shock-induced separation in Bethe–Zel'dovich–Thompson fluids. J. Fluid Mech. **393**, 1–21 (1999)

Cramer, M., Tarkenton, G.: Transonic flows of Bethe–Zel'dovich–Thompson fluids. J. Fluid Mech. **240**, 197–228 (1992)

Duan, L., Beekman, I., Martin, M.: Direct numerical simulation of hypersonic turbulent boundary layers. Part 3. Effect of Mach number. J. Fluid Mech. **672**, 245–267 (2011)

Ducros, F., Ferrand, V., Nicoud, F., Weber, C., Darracq, D., Gacherieu, C., Poinsot, T.: Large-eddy simulation of the shock/turbulence interaction. J. Comput. Phys. **152**(2), 517–549 (1999)

Eitel-Amor, G., Örlü, R., Schlatter, P.: Simulation and validation of a spatially evolving turbulent boundary layer up to Re_θ=8300. Int. J. Heat Fluid Flow. **47**, 57–69 (2014)

Franko, K.J., Lele, S.K.: Breakdown mechanisms and heat transfer overshoot in hypersonic zero pressure gradient boundary layers. J. Fluid Mech. **730**, 491–532 (2013)

Gloerfelt, X., Robinet, J.C., Sciacovelli, L., Cinnella, P., Grasso, F.: Dense-gas effects on compressible boundary-layer stability. J. Fluid Mech. **893**, A19 (2020). https://doi.org/10.1017/jfm.2020.234

Gloerfelt, X., Cinnella, P.: Large eddy simulation requirements for the flow over periodic hills. Flow Turbul. Combust. **103**(1), 55–91 (2019)

Huang, P., Coleman, G., Bradshaw, P.: Compressible turbulent channel flows: DNS results and modelling. J. Fluid Mech. **305**, 185–218 (1995)

Jameson, A., Schmidt, W., Turkel, E.: Numerical solution of the euler equations by finite volume methods using Runge–Kutta time stepping schemes. In: 14th Fluid and Plasma Dynamics Conference, p. 1259 (1981)

Kawai, H., Terashima, H., Negishi, H.: A robust and accurate numerical method for transcritical turbulent flows at supercritical pressure with an arbitrary equation of state. J. Comput. Phys. **300**, 133–160 (2015)

Kim, J.W., Lee, D.J.: Adaptive nonlinear artificial dissipation model for computational aeroacoustics. AIAA J. **39**(5), 810–818 (2001)
Kluwick, A.: Interacting laminar boundary layers of dense gases. Fluid Gasdyn. Acta Mech. **4**, 335–349 (1994)
Lund, T., Wu, X., Squires, K.: Generation of turbulent inflow data for spatially-developing boundary layer simulations. J. Comput. Phys. **140**, 233–258 (1998)
Martin, J., Hou, Y.: Development of an equation of state for gases. AIChE J. **1**(2), 142–151 (1955)
Pirozzoli, S., Bernardini, M.: Turbulence in supersonic boundary layers at moderate Reynolds number. J. Fluid Mech. **688**, 120–168 (2011)
Poggie, J., Bisek, N.J., Gosse, R.: Resolution effects in compressible, turbulent boundary layer simulations. Comput. Fluids **120**, 57–69 (2015)
Poling, B., Prausnitz, J., O'Connell, J., Reid, R.: The Properties of Gases and Liquids, vol. 5. McGraw-Hill, New York (2001)
Schlatter, P., Örlü, R.: Assessment of direct numerical simulation data of turbulent boundary layers. J. Fluid Mech. **659**, 116–126 (2010)
Sciacovelli, L., Cinnella, P., Content, C., Grasso, F.: Dense gas effects in inviscid homogeneous isotropic turbulence. J. Fluid Mech. **800**, 140–179 (2016)
Sciacovelli, L., Cinnella, P., Gloerfelt, X.: Direct numerical simulations of supersonic turbulent channel flows of dense gases. J. Fluid Mech. **821**, 153–199 (2017)
Sciacovelli, L., Cinnella, P., Grasso, F.: Small-scale dynamics of dense gas compressible homogeneous isotropic turbulence. J. Fluid Mech. **825**, 515–549 (2017)
Smits, A.J., Matheson, N., Joubert, P.N.: Low-Reynolds-number turbulent boundary layers in zero and favorable pressure gradients. J. Ship Res. **27**(3), 147–157 (1983)
Smits, A., Monty, J., Hultmark, M., Bailey, S., Hutchins, N., Marusic, I.: Spatial resolution correction for wall-bounded turbulence measurements. J. Fluid Mech. **676**, 41–53 (2011)
Spinelli, A., Cammi, G., Gallarini, S., Zocca, M., Cozzi, F., Gaetani, P., Dossena, V., Guardone, A.: Experimental evidence of non-ideal compressible effects in expanding flow of a high molecular complexity vapor. Exp. Fluids **59**(8), 126 (2018)
Thompson, P.: A fundamental derivative in gasdynamics. Phys. Fluids **14**(9), 1843–1849 (1971)
Thompson, K.: Time dependent boundary conditions for hyperbolic systems. J. Comput. Phys. **68**(1), 1–24 (1987)
Trettel, A., Larsson, J.: Mean velocity scaling for compressible wall turbulence with heat transfer. Phys. Fluids **28**(2), 026102 (2016)
Van Driest, E.R.: The problem of aerodynamic heating. Aeronaut. Eng. Rev. **15**, 26–41 (1956)
Walz, A.: Boundary Layers of Flow and Temperature. MIT Press, Cambridge (1969)
Wenzel, C., Selent, B., Kloker, M., Rist, U.: DNS of compressible turbulent boundary layers and assessment of data scaling-law quality. J. Fluid Mech. **2018**, 428–468 (2018)
Wu, X.: Inflow turbulence generation methods. Annu. Rev. Fluid Mech. **49**, 23–49 (2017)
Zamfirescu, C., Dincer, I.: Performance investigation of high-temperature heat pumps with various BZT working fluids. Thermochim. Acta **488**, 66–77 (2009)
Zhang, X., Watanabe, T., Nugata, K.: Turbulent/nonturbulent interfaces in high-resolution direct numerical simulation of temporally evolving compressible turbulent boundary layers. Phys. Rev. Fluids **3**, 094605 (2018)
Zocca, M., Guardone, A., Cammi, G., Cozzi, F., Spinelli, A.: Experimental observation of oblique shock waves in steady non-ideal flows. Exp. Fluids **60**(6), 101 (2019)

Affiliations

Luca Sciacovelli[1] · Xavier Gloerfelt[1] · Donatella Passiatore[1] · Paola Cinnella[1] · Francesco Grasso[2]

Xavier Gloerfelt
xavier.gloerfelt@ensam.eu

Donatella Passiatore
donatella.passiatore@ensam.eu

Paola Cinnella
paola.cinnella@ensam.eu

Francesco Grasso
francesco.grasso@lecnam.net

[1] DynFluid Laboratory, Arts et Métiers ParisTech, Paris, France

[2] DynFluid Laboratory, Conservatoire National des Arts et Métiers, Paris, France